

Microfabrication of coupled fluid–structure systems with applications in acoustic sensing

Robert D. White^{a,*}, Lei Cheng^b, Karl Grosh^b

^a *Tufts University, Medford, MA 02155, USA*

^b *University of Michigan, Ann Arbor, MI 48109, USA*

Received 15 May 2007; received in revised form 9 August 2007; accepted 30 August 2007

Available online 8 September 2007

Abstract

A fabrication process for manufacturing coupled fluid–structure microsystems is described. This process allows production of a novel class of trapped-fluid acoustic sensors. The systems consist of wafer-thick fluid chambers bounded by arbitrarily shaped membranes. A stacked film structure of silicon nitride and boron doped polysilicon is used to reduce residual stresses in the membranes. Tin–gold fluxless solder bonding is used to fabricate capacitive structures which allow electrical sensing of membrane vibrations. An acoustic sensor fabricated using this process is demonstrated. An equivalent acoustic circuit model for the system is described, and models the low-frequency system response accurately. Experimental measurements of sensitivity, noise density, and linearity are presented.

© 2007 Elsevier B.V. All rights reserved.

Keywords: MEMS; Microphone; Acoustic; Sensor; Microfabrication

1. Introduction

A fabrication process and mathematical modeling framework has been developed for the production of trapped-fluid microsystems. These structural-acoustic systems consist of a wafer-thick fluid chamber coupled to multiple arbitrarily shaped membranes. A two stage backside deep reactive ion etching (DRIE) process is used to produce the fluid chamber, and to define the shape of the membranes. The membranes themselves are silicon nitride/p++ polysilicon/silicon nitride laminates which have a low net tensile stress, are electrically conducting, and yet are electrically isolated both from the environment and the trapped fluid. Sn–Au fluxless solder bonding is used to attach a top Pyrex glass cover which incorporates a Cr/Pt top electrode. This results in a structure which is capacitively coupled to the membranes and can be used for sensing or actuation. As the small capacitive gap is defined by a dry bonding step at the end of the process, there are no problems with in-process stiction, a problem which is often associated with large area membranes and narrow sense gaps.

Development of the fabrication process was motivated by the authors' ongoing efforts to produce lifelike micromachined cochlear models and biomimetic cochlear-like sensors [1–3]. In order to accomplish this task, a fabrication process was required to produce a deep (wafer thick), fluid-filled chamber coupled to an exponentially tapered membrane. In addition, multiple sensing structures needed to be integrated into the structure to measure vibration of the membrane in response to traveling fluid–structure waves. For additional details on hydromechanical cochlear models, see work by the authors [1–3] and other researchers [4–7].

In this paper, we report a trapped-fluid acoustic structure with a single sensing channel. This structure is not cochlear-like, as it does not have a long, tapered membrane with variable compliance. Nor does it have multiple sensing channels. Rather, the sensor system was built to demonstrate the feasibility of the new fabrication process at producing a trapped-fluid microstructure with integrated capacitive sensing.

To our knowledge, there is no example of other trapped-fluid micromachined acoustic sensors in the literature. However, single channel micromachined capacitively sensed microphones have been designed and constructed by a number of researchers [8–11]. The sensor that we have produced differs from the traditional design by sealing the backing cavity and filling it with a

* Corresponding author. Tel.: +1 617 627 2210.

E-mail address: r.white@tufts.edu (R.D. White).

liquid, in this case silicone oil, rather than air. This has two primary effects. First, it increases the dynamic mass of the sensor. This reduces the frequency of the primary resonance, thereby reducing bandwidth. In addition, since more of the dynamic mass comes from the trapped fluid, the mass loading from the environment has less effect on the sensor dynamics, reducing sensitivity to the density of the environment. Secondly, as in the cochlea, the fluid serves as an acoustic transmission medium, allowing the acoustic input to be located at a physically remote location from the location at which measurements occur.

In addition, fabrication of the backing cavity in many of these earlier devices was accomplished using anisotropic liquid-phase etching of silicon by potassium hydroxide solutions (KOH). Due to the cubic symmetry of the single crystal silicon structure, use of an anisotropic etchant such as KOH restricted the membrane to a rectangular shape. In addition, the shape of the backing cavity that was formed behind the membrane was completely determined by the shape of the membrane. The fabrication process described here is not constrained in these ways.

Following a description of the fabrication process, a mathematical model of the system is presented. The model captures the low frequency physics in a very efficient manner. Pre-tension in the membrane, fluid loading from the trapped fluid, and squeeze film damping in the air gap are included in the model. Model predictions are compared to experimental measurements

of the system frequency response with good agreement at low frequencies (below 2 kHz).

2. Design

Before proceeding to a description of the fabrication process, a brief description of the system design is given to aid in visualization. The mechanical portion of the sensor, diagrammed in Fig. 1, is a square silicon die 1.25 cm on a side. It consists of a 0.52 mm deep, 10 mm diameter fluid chamber, filled with silicone oil of 200 cSt viscosity. This chamber is constrained on one side by a series of flexible membranes. The center membrane is circular with a 2.5 mm diameter. Arrayed around the outer portions of the chamber are two rings of eight arc segments, each subtending 30°, with inner and outer diameters as shown in the figure. The bottom side of the chamber is sealed by a square Pyrex die 1.25 cm on a side. On the top side, a smaller square Pyrex glass die, 5 mm on a side, is bonded over the center of the silicon chip. A thin film Cr/Pt electrode on the bottom side of the Pyrex forms a parallel plate capacitor with the central circular membrane.

Incoming sound excites motion of the outer “input” membranes, generating an acoustic pressure in the fluid chamber. This causes deflection of the center “sensing” membrane. With a dc bias applied between the Cr/Pt electrode and the “sensing”

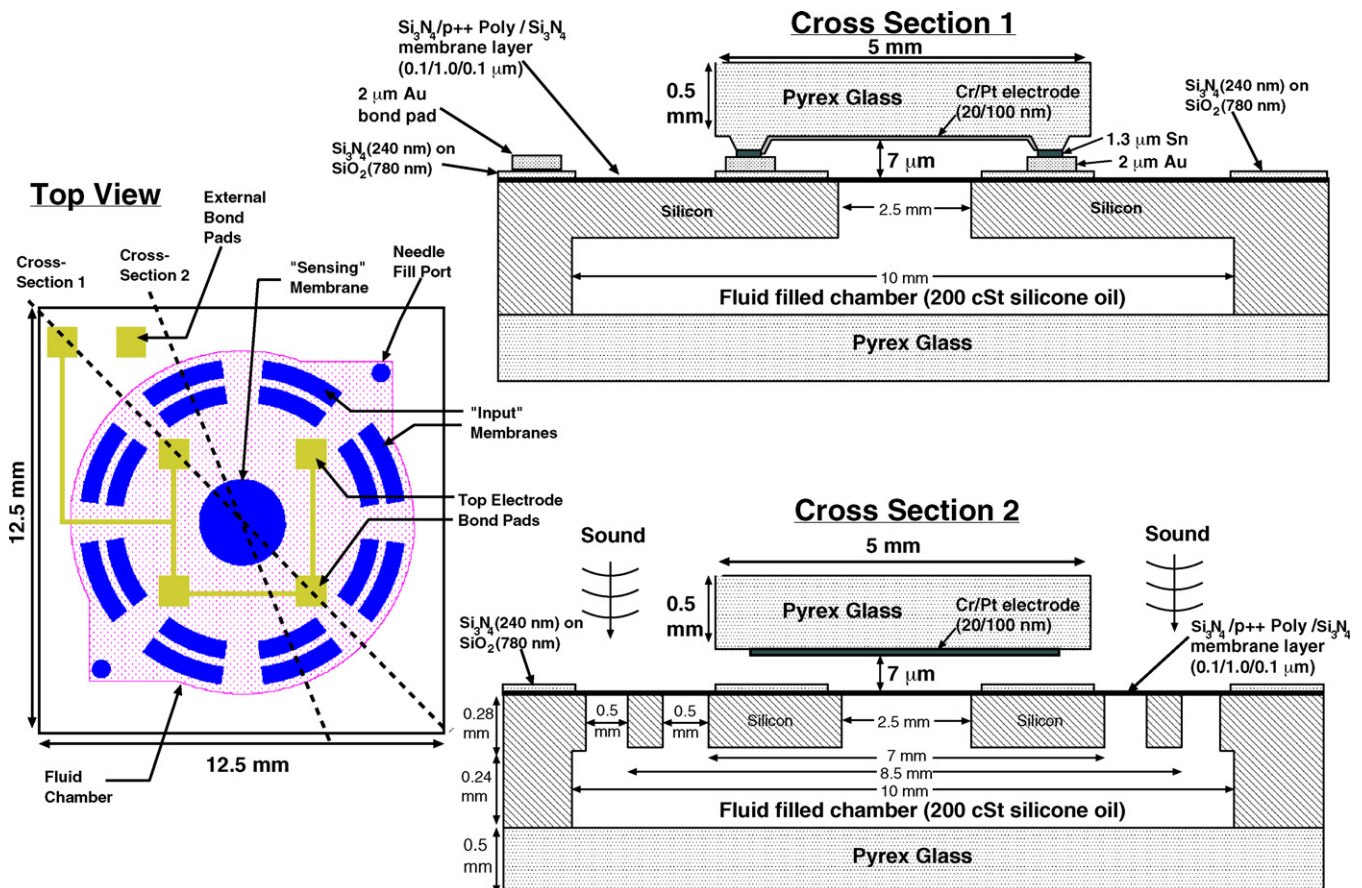


Fig. 1. Conceptual diagram of the sensor system. The top view (on the left) shows the layout of the metallization, the location of the flexible membranes, and the location of the bonding pads. Two cross-sections (on the right) show the geometry of the fluid chamber and the thickness of the various thin films.

membrane, deflections result in charge generation. The charge is integrated by a charge amplifier to produce a voltage output.

3. Fabrication

The sensors were fabricated at the University of Michigan Nanofabrication Facility. The process is diagrammed in Fig. 3. The starting substrates were double-side polished 100 mm diameter, 520 μm thick, (1 0 0) oriented, p-type (1–10 $\Omega\text{ cm}$) silicon wafers. After cleaning, the wafers were oxidized using pyrogenic oxidation at 1100 $^{\circ}\text{C}$, producing 2 μm of thermal SiO_2 . A structural laminate of silicon nitride/p++ polysilicon/silicon nitride (0.1/1.0/0.1, μm) was then deposited. The nitride layers are stoichiometric nitrides deposited by LPCVD. The polysilicon is fine grained LPCVD polysilicon with compressive residual stress deposited at 588 $^{\circ}\text{C}$ and 100 mT. Solid-source boron diffusion at 1175 $^{\circ}\text{C}$ was used to dope the polysilicon to the solid solubility limit. The borosilicate glass which grew on the polysilicon during boron deposition was then stripped in 49% HF. Finally, an insulating layer consisting of 0.78 μm of LPCVD SiO_2 followed by 0.24 μm of LPCVD Si_3N_4 was deposited.

The backside films were removed and the backside oxide patterned as an etch mask for the fluid chamber, as shown in Fig. 3, step 1a. The two top dielectric layers were then removed from the device regions, and vias were etched through to the polysilicon. Cr/Au metallization (50 nm and 2 μm , respectively) was

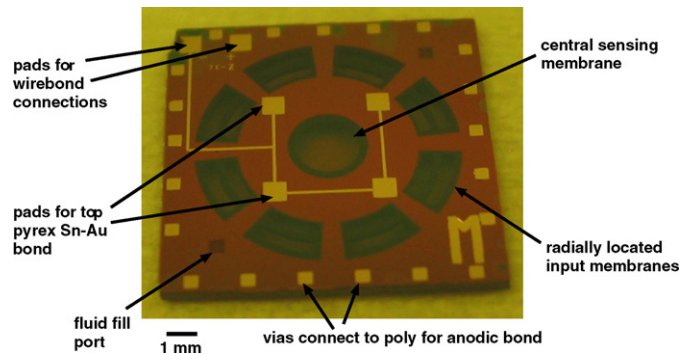


Fig. 2. Photograph of a chip after through-etch and cleaning, but before bonding.

sputtered on and patterned to provide bonding pads for the top Pyrex piece, connections to the package, and electrical connection through the vias to the polysilicon layer. The geometry can be seen in the photograph of Fig. 2 and the diagram of Fig. 3, step 2a.

The first of two deep-trench RIE (DRIE) etches was performed in an STS tool running a modified Bosch process. The etch was 300 μm deep and defined the shape of the membranes, as seen in Fig. 3, step 3a. Thick photoresist was then spun onto the front side of the process wafers and the wafers were broken up into individual dies along trenches etched during the first DRIE etch. The dies were mounted around the outside of

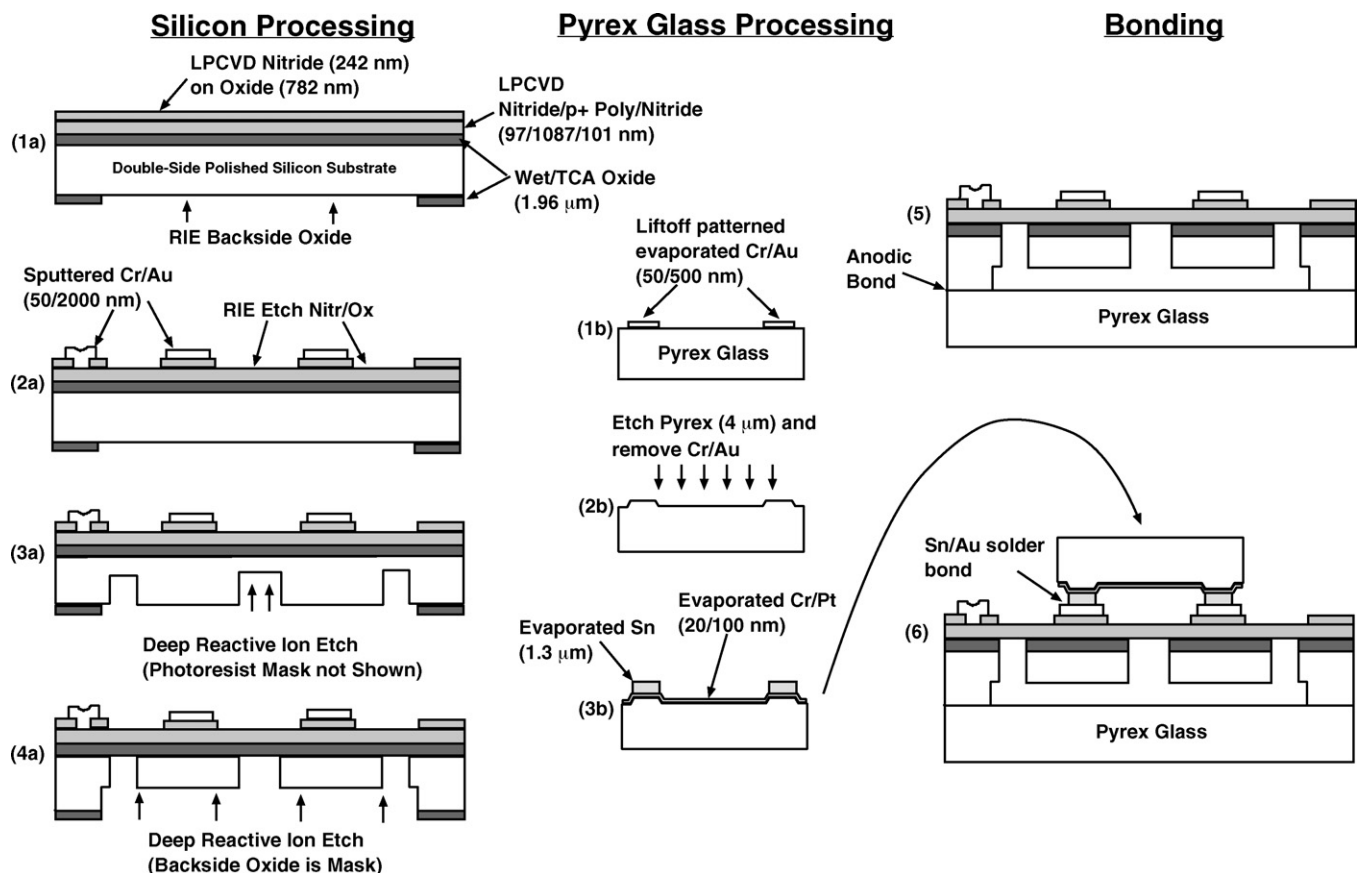


Fig. 3. Diagram of the microfabrication process. The left-hand column shows the process for fabricating the main silicon die. The center column shows the process for fabricating the Pyrex top cap. The right-hand column shows the two bonding steps.

a silicon handle wafer with additional photoresist, and a second DRIE etch was performed, using the backside SiO_2 as an etch mask, and stopping on the buried $2\text{ }\mu\text{m}$ SiO_2 . The situation at this point is seen in Fig. 3, step 4a.

The motivation for cleaving the wafers into dies prior to the final DRIE etch was twofold: (1) at this stage, the structures are still thick and robust and can withstand the mechanical shock of the cleaving process. (2) The DRIE etch rate is non-uniform, with faster etch rates near the edge of the wafer. By mounting the dies around the outside of a handle wafer, a more uniform etch is achieved, reducing the danger of breaking the surface membranes due to overetch.

The dies, which were still attached to the handle wafer, were then dipped in isopropyl alcohol for 10 s and immediately transferred to 1:1 HF (49%): H_2O to remove the remains of the SiO_2 etch stop. The isopropanol dip was needed to avoid air bubbles attaching to the silicon surface and interfering with the etch.

After cleaning and drying, the membranes for the single-channel dies appeared flat ($<0.1\text{ }\mu\text{m}$ deflection) under a white light interferometer. Fig. 2 shows a photograph of a sensor chip at this stage. Fig. 4 shows scanning electron microscope images of a cross-section of the structure. Chamfering of the sharp corners

is seen where the narrow membrane-defining etch meets the chamber etch. Some particles are seen in the sense gap in the figure; we believe that these particles were generated during the dicing process used to cut the die and produce the cross-section. Particles were not present in the tested devices.

In parallel with the silicon processing, a $500\text{ }\mu\text{m}$ thick, 100 mm diameter Pyrex glass wafer (Corning type 7740 borosilicate glass) was processed to produce the top electrodes. The Pyrex was etched in 3:1 $\text{H}_2\text{O}:\text{HF}$ (49%) to produce the spacer “legs” using an evaporated $50/500\text{ nm}$ Cr/Au etch mask, for a final etch depth of $4\text{ }\mu\text{m}$. The process is diagrammed in Fig. 3, steps 1b and 2b. The etch exhibited significant undercut, with an undercut on the order of $100\text{ }\mu\text{m}$ for a $4\text{ }\mu\text{m}$ deep etch (the undercut varied considerably from wafer to wafer). For this process, the undercut is advantageous, as it leads to a gentle slope up the side of the leg, aiding in deposition of metal interconnects. Following the etch, the Cr/Au etch mask was removed using wet etching, and Cr/Pt ($20/100\text{ nm}$) electrodes were evaporated on and patterned via liftoff. Sn “bumps” $1.3\text{ }\mu\text{m}$ high were also evaporated on and patterned via liftoff. The finished glass die is shown in Fig. 3, step 3b. A second unpatterned Pyrex wafer was diced into 12.5 mm square pieces to serve as a back cap, and cleaned using 3:1, $\text{H}_2\text{SO}_4:\text{H}_2\text{O}_2$.

Once all the dies were prepared, the two final bonding steps shown in Fig. 3, steps 5 and 6 were conducted. First, the silicon dies were bonded to the unpatterned backside glass pieces using anodic bonding. The bond was carried out in a custom bonding jig, which made contact only around the outside of the die, protecting the fragile membrane structures in the center. The bond was performed in a N_2 ambient at atmospheric pressure and 330°C with a 700 V dc bias for 30 min [12].

The topside, patterned Pyrex dies were then bonded to the silicon using Sn–Au solder bonding. The use of a dry Sn–Au solder bond process for the microphone top plate assembly is a novel approach for avoiding problems with in-process stiction. These problems are often associated with wet etching of sacrificial layers in a thin gap. The bond was performed in another custom bonding jig in an N_2 ambient at atmospheric pressure and 350°C . Clamping pressure of 100 MPa was applied at the interface. Fig. 5 shows microscope pictures of a successful bond; for a successful bond, the Sn is seen to visibly diffuse into the Au. For more details of Sn–Au bonding, see Goyal et al. [13], Matijasevic et al. [14], and Lee and Wang [15].

In a final packaging step, needles were epoxied into the fluid fill ports, and a micrometer injection jig was used to inject silicone oil into the fluid chamber. The needles were cut off and the inlet and outlet ports were sealed with epoxy. The use of high viscosity silicone oil (200 cSt was used) improved the ability to fill the chamber without generation of bubbles. The glass backside allowed the chamber to be observed during filling, so that any bubbles that did form could be forced out by continuing to flow silicone oil through the chamber. The finished device was finally mounted in a hybrid leadless ceramic chip carrier (LCCC) package and wire-bonded using Au wires. A photograph of the finished sensor is shown in Fig. 6.

The residual stress in the membrane is a critical parameter for determining device performance. Three techniques were

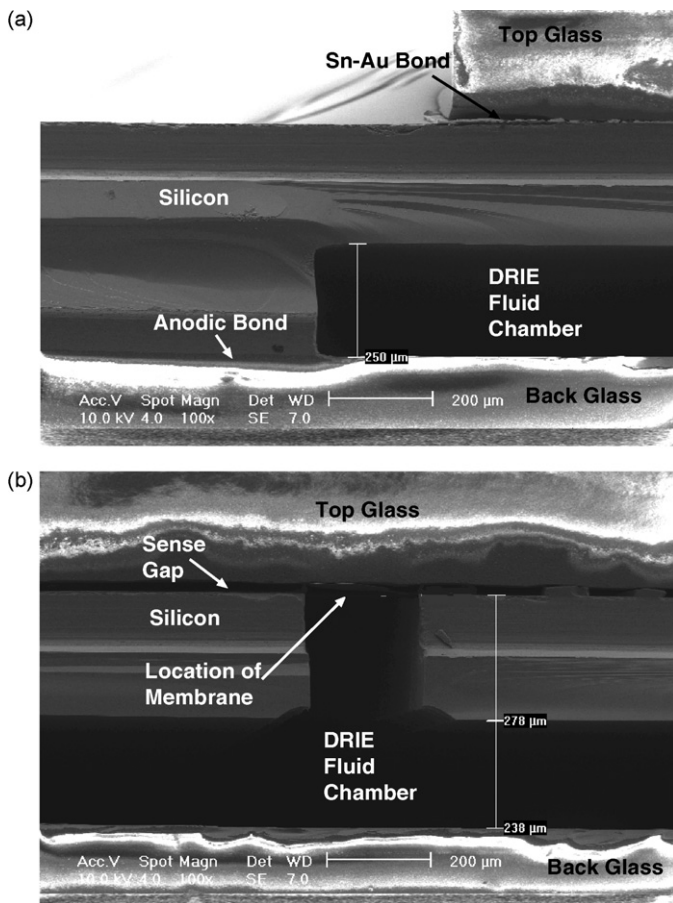


Fig. 4. Scanning electron microscope pictures of a cross-section of a similar device (from the same wafer) at the end of processing. (a) The main part of the fluid chamber, $250\text{ }\mu\text{m}$ deep, showing the anodic bond to the back glass, and the Sn–Au bond to the top glass. (b) The narrow part of the fluid chamber leading to the membrane, which extends to the full wafer thickness.

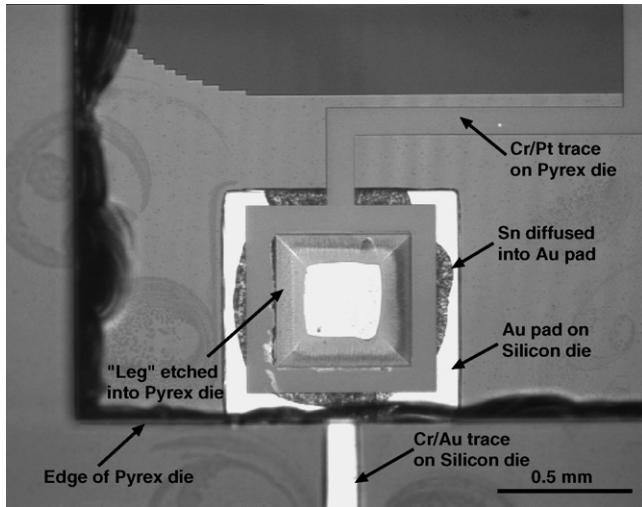


Fig. 5. Light microscope picture showing a Sn–Au bond. The view is through the top Pyrex to the silicon. In a successful bond, the Sn is seen to diffuse into the Au around the edges of the bond.

applied to estimate the membrane stress: wafer curvature measurements, *in-situ* strain gauges [16], and capacitive snapdown voltage measurements. Wafer curvature for a monitor wafer processed alongside the device wafer shows an average tension of 52 N/m with a standard deviation of 16 N/m. The minimum tension was 12 N/m and the maximum 100 N/m. Fig. 7 shows the stress variation across the wafer.

In-situ strain gauges were fabricated on the process wafer; the design was taken from Zhang et al. [16]. A SEM image of the strain gauge is shown in Fig. 8. The tip deflection indicates 50 MPa tensile stress (60 N/m tension) for the process wafer, which agrees with the wafer curvature measurements. For the particular device described in this paper, snapdown occurred at 22 V, indicating a tension of 12 N/m, at the low end of the expected range, but within the variation seen by wafer curvature.

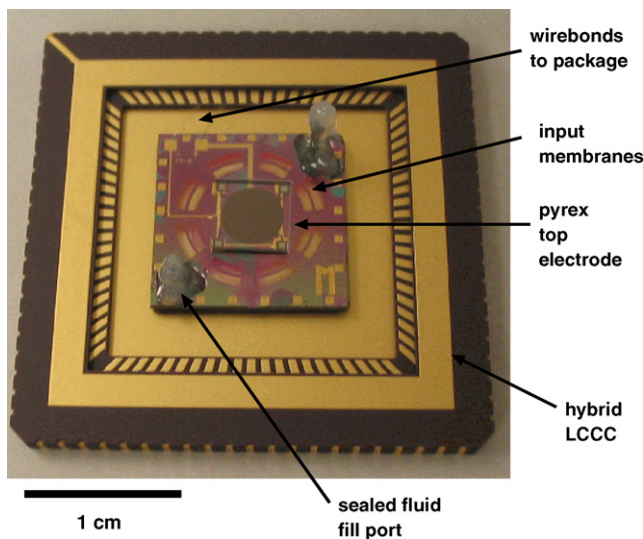


Fig. 6. Photograph of a finished sensor. This top view shows the outer ring of “input” membranes, the bonded Pyrex plate with top electrode, the fluid inlet and outlet, and the electrical wire-bond connections.

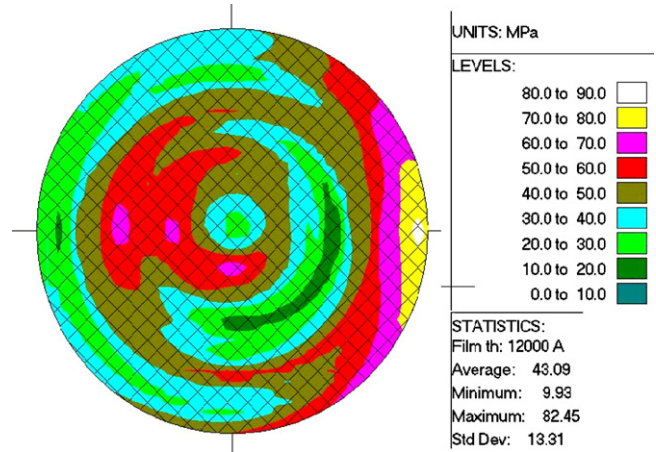


Fig. 7. Results of wafer curvature measurements for a monitor wafer processed alongside the process wafers. The silicon nitride/boron doped polysilicon/silicon nitride laminate, 0.1 μm /1.0 μm /0.1 μm in thickness, achieves an average tensile stress of 43 MPa, which corresponds to 52 N/m tension for a 1.2 μm thick film.

4. Model

Mathematical modeling of system response requires solution of a coupled fluid–structure interaction problem. There are two fluid domains: the trapped silicone oil inside the device, and the air in the gap between the top glass and the central membrane. The flexible structure is the nitride/polysilicon/nitride laminate, which is isotropic and under tensile residual stress. The input to the system is an acoustic pressure presented to the input membranes around the outside of the device. The result of the computation is the oscillatory deflection of the central circular membrane, which can be converted into an electrical output.

At low frequencies where the sensor dimensions are small compared to the wavelength of interest, a lumped element model is appropriate to approximate the sensitivity of the device [8,9,17]. This model maintains the appropriate couplings

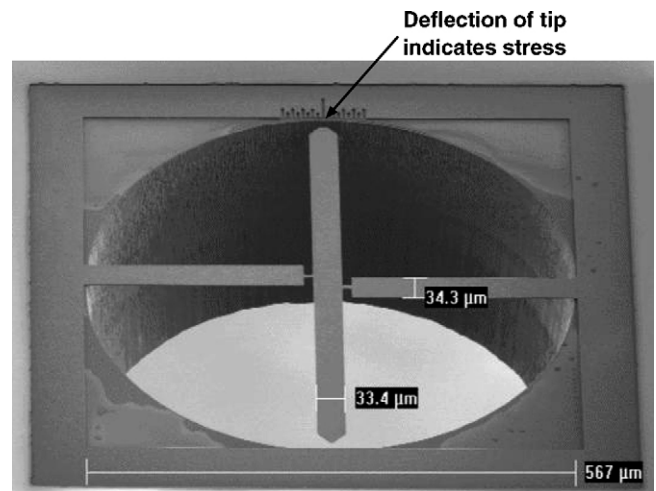


Fig. 8. Scanning electron microscope picture of a released *in-situ* strain gauge. The tip displacement is approximately 2.5 μm , indicative of approximately 50 MPa stress, which is comparable with the results obtained from wafer curvature measurements [16].

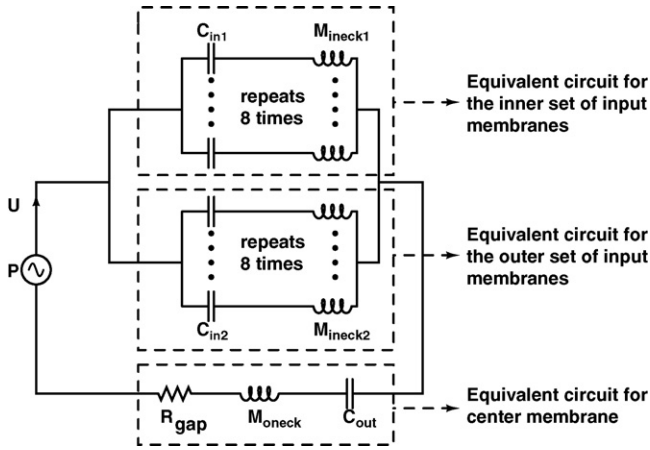


Fig. 9. Equivalent acoustic circuit model for the system. Voltage is equivalent to acoustic pressure, P , and current is equivalent to volume velocity, U .

between the structure and the fluid domains. The lumped element model, however, assumes that all structural elements deflect in a shape similar to their first *in vacuo* structural modeshape. It also assumes that there is little spatial variation in pressure in either of the fluid domains. At high frequencies both of these assumptions will begin to break down as more spatial variation occurs in both pressure and structural deflection.

The lumped element model is expressed as an equivalent circuit model for the system, shown in Fig. 9. Voltage is equivalent to acoustic pressure, and current is equivalent to volume velocity. Capacitors represent compliance, inductors represent inertia, and resistors represent damping. A minimum set of components have been chosen which represent the essential physics of the problem.

The inertias in the equivalent circuit model come entirely from the mass of the heavy fluid (silicone oil) inside the micromachined cavity. The effective mass of the trapped fluid dominates the small mass of the membranes. M_{ineck1} is the neck mass under one of inner membranes, M_{ineck2} the neck mass under one of outer membranes, and M_{oneck} is the neck mass under the central sensing membrane. For all these neck masses, since one end is terminated in a large fluid cavity, the end correction is added [17]. This results in

$$M = \rho_f \frac{L + 0.85r_{eff}}{A} \quad (1)$$

where ρ_f is the density of the silicone oil (950 kg/m^3), A the cross-sectional area of the neck, and r_{eff} is the effective neck radius, $r_{eff} = \sqrt{A/\pi}$. One of the unique features of this design is that the trapped fluid mass also dominates the radiation mass of the fluid environment, even for a heavy fluid like water. The radiation mass can be estimated as

$$M_{rad} = \frac{8\rho_{env}}{3\pi^2 r_{eff}} \quad (2)$$

where ρ_{env} is the density of the fluid environment (usually air or water). Even for a heavy fluid like water, this added radiation mass is small compared to the neck masses and has little influence on the physics. Hence, it is not included in the model.

The compliances of the various membranes are computed assuming that tension dominates bending stiffness, which is valid for these large area, thin, tensioned membranes.

The diaphragm compliance can be derived from the fundamental mode of the membrane vibration equation,

$$T \left(\frac{\partial^2 \psi}{\partial r^2} + \frac{1}{r} \frac{\partial \psi}{\partial r} + \frac{1}{r^2} \frac{\partial^2 \psi}{\partial \theta^2} \right) - \rho_m \frac{\partial^2 \psi}{\partial t^2} = 0 \quad (3)$$

where T and ρ_m are the tension and the area density of the membrane, respectively. In order to satisfy the boundary conditions, the fundamental mode of an input membrane is

$$\psi_{in1}(r, \theta) = \sin \left(\frac{\pi(\theta - \theta_1)}{\theta_2 - \theta_1} \right) (J_6(kr) + BY_6(kr)) \quad (4)$$

where the constant B and the value of k are determined numerically to satisfy the boundary conditions $\psi_{in1}(r = r_1) = \psi_{in1}(r = r_2) = 0$. r_1 and r_2 are the inner and outer radii of the input membrane. $\theta_1 = 0$ and $\theta_2 = \pi/6$ are the arc angles which delineate the membrane edges. J_6 and Y_6 are Bessel functions of the first and second kind of order 6.

Assuming the static deflection of the membrane is

$$w = A \psi_{in1} \quad (5)$$

and substituting into the static membrane equation,

$$T \left(\frac{\partial^2 w}{\partial r^2} + \frac{1}{r} \frac{\partial w}{\partial r} + \frac{1}{r^2} \frac{\partial^2 w}{\partial \theta^2} \right) = P \quad (6)$$

we can solve for the coefficient A which depends linearly on the pressure P . The membrane compliance is then defined as the ratio of the volume displacement (the area integral of w) to the applied pressure, which can be expressed as

$$C_{in1} = \frac{(\int_{r_1}^{r_2} \int_{\theta_1}^{\theta_2} \psi_{in1} r dr d\theta)^2}{Tk^2 (\int_{r_1}^{r_2} \int_{\theta_1}^{\theta_2} \psi_{in1}^2 r dr d\theta)} \quad (7)$$

This integral expression was evaluated numerically to compute each of the input membrane compliances. Note that C_{in1} and C_{in2} have the same form, but different values of k , B , r_1 and r_2 .

In Fig. 9, C_{out} is the acoustic compliance of the center membrane. For this circular membrane, the fundamental mode is $\psi_2 = J_0(k_2 r)$, where J_0 is the first kind Bessel function of order 0. k_2 is determined numerically (or from tables) from the boundary condition $\psi_2(r = r_c) = 0$, where r_c is the radius of the center membrane. The acoustic compliance is computed numerically from the same area integral,

$$C_{out} = \frac{(2\pi \int_{r_1}^{r_2} \psi_2 r dr)^2}{Tk_2^2 (2\pi \int_{r_1}^{r_2} \psi_2^2 r dr)} \quad (8)$$

Damping in the system model comes entirely from the squeeze film damping of the sense gap. The solution of the isothermal compressible gas-film Reynolds equation as a model for squeeze film damping has been discussed by a number of authors [18–21]. The force generated by uniform motion of a circular

plate of radius R is given in Starr [19],

$$F_D = \frac{3\pi\eta R^4 jv}{2g^3} \quad (9)$$

where g is the fluid gap height, v the uniform velocity of the disk, and η is the fluid shear viscosity. Recasting this as an acoustic resistor, assuming that the total force on the circular membrane can be approximated by the solution for a uniform circular disk with the same volume velocity,

$$R_{\text{gap}} = \frac{3\eta}{2\pi g^3} \quad (10)$$

Note that the trapped fluid has two primary effects. First, it acts as a transmission medium for acoustic energy to travel from the input membranes to the sensing membrane. Even though the fluid is essentially incompressible, as the wavespeed is high and the dimensions are small, it nevertheless acts as a transmission medium, allowing the various membranes to couple acoustically. Secondly, the heavy-trapped fluid is the primary source of system mass.

Compliance of the fluid cavity due to compressibility of the trapped fluid is small compared to the membrane compliance, and has no significant effect. The chamber acoustic compliance at low frequencies is

$$C_{\text{cavity}} = \frac{1}{\rho_f c^2} V_{\text{cavity}} \quad (11)$$

where V_{cavity} is the volume of the cavity, ρ_f the density of the silicone oil, and c is the wavespeed in the silicone oil (estimated at 1000 m/s based on tabulated wavespeeds in other oils [22]). This cavity compliance can be included in the model in parallel with the equivalent circuit for the output membrane. It has no observable effect on model predictions, as the trapped fluid is nearly incompressible in comparison with the membranes. Also, any damping coming from the viscosity of the trapped fluid has been neglected.

From this acoustic circuit, we can relate the volume velocity of the sensing membrane U to the acoustic pressure input P . Due to the use of the first kind Bessel function of order zero, the center point displacement is related to the volume velocity by

$$w(r=0) = \frac{2.32}{j\omega A_{\text{out}}} U \quad (12)$$

The parameters given in Table 1 were used in computing the system response. The fluid density was measured on a balance.

Table 1
Properties used for the lumped element computation

Parameter	Value
Fluid density, ρ_f (kg/m ³)	950
Neck height, L (μm)	278
Air gap, g (μm)	7
Bias voltage, V_b (V)	9
Air viscosity, η ($\mu\text{Pa s}$)	18.5
Permittivity, ϵ_0 (pF/m)	8.854
Structure tension, T (N/m)	12

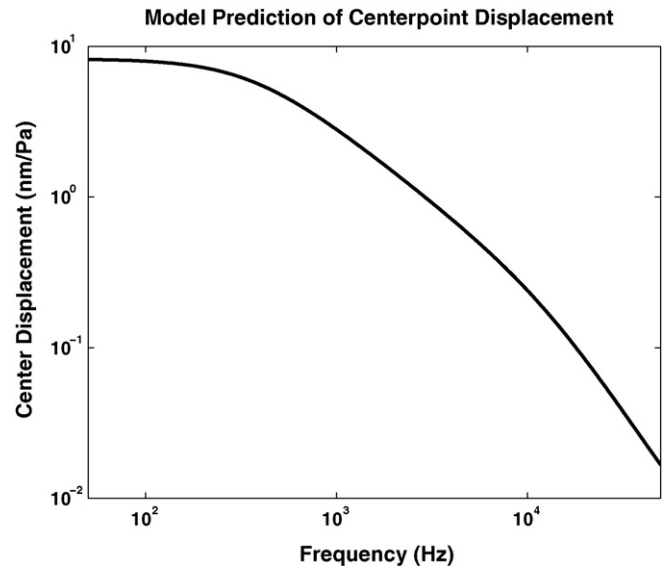


Fig. 10. Frequency response function for the predicted magnitude of center point displacement relative to driving pressure on the input membranes.

The neck height of the trapped fluid is taken from the SEM picture shown in Fig. 4. The air gap height, g , is determined from the change in static capacitance when the top glass is bonded on, and matches with the expected gap of 7 μm based on the fabrication process. The bias voltage is the 9 V applied voltage. The air viscosity is a standard number [22], and the permittivity of free space is a physical constant.

The most difficult parameter to determine in the model is the structure tension, T . As discussed earlier, the average tension for the wafer was 52 N/m, the minimum tension was 12 N/m, and the maximum 100 N/m. For the particular device modeled here, $T = 12$ N/m was used based on snapdown measurements.

Fig. 10 shows the predicted sensing membrane center point displacement in response to driving pressure on the input membranes. The response sensitivity has a -3 dB bandwidth (based on center point displacement) of 400 Hz. MEMS devices usually have a wider bandwidth; the low bandwidth for this system is due to the added mass from the trapped fluid. The low bandwidth could be an advantage or disadvantage, depending on the application. Higher rolloff frequencies can be achieved by using smaller or more highly tensioned membranes, at the cost of a reduced low frequency sensitivity. Note also from the modeled response that there is no observable resonant peak in the frequency response; the system is highly damped by the squeeze film damping.

5. Experimental results

A simplified schematic of the system electronics is given in Fig. 11. An AD795 low noise precision FET input operational amplifier was configured as a charge amplifier to integrate the charge generated by the MEMS sensor. A 10 pF silvered mica capacitor was used as the feedback capacitor and sets the charge gain of the system. A 200-M Ω feedback resistor was used to stabilize the system at dc. The low frequency RC cutoff frequency

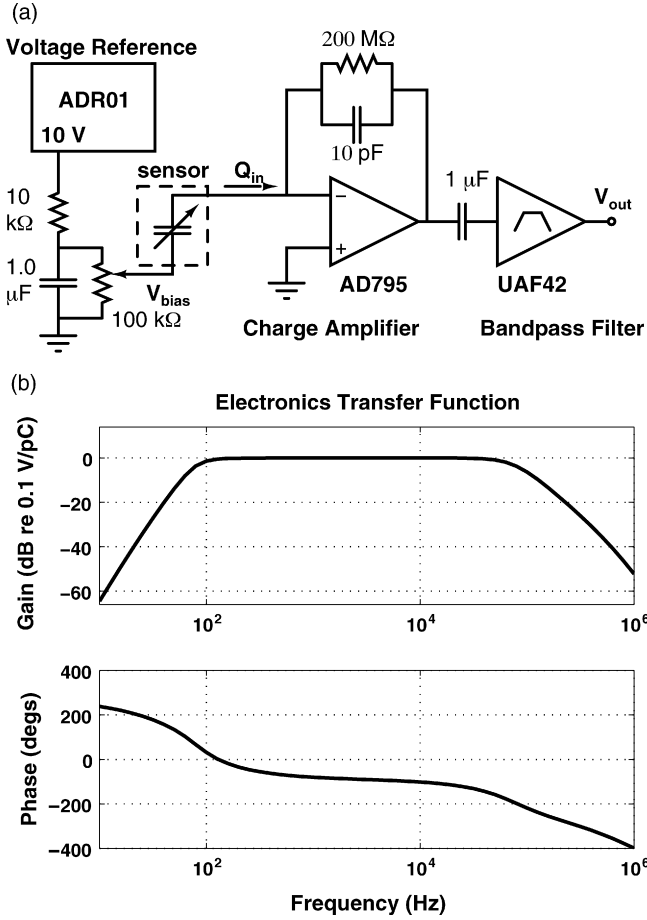


Fig. 11. (a) Schematic of the system electronics, including dc voltage reference, charge amplifier, and bandpass filter. (b) Charge amp and bandpass filter characteristics (V_{out} vs. Q_{in}).

for this combination is 80 Hz. The 10-pF capacitor results in a 0.1 V/pC charge sensitivity. The output of the charge amplifier passes through a 1-μF coupling capacitor into a bandpass filter circuit. The filter was constructed using a UAF42 universal active filter chip from Texas Instruments. The first stage was configured as a lowpass state-variable filter with a two pole cutoff at 70 kHz. The second stage was configured as a highpass voltage controlled voltage source with a 80 Hz cutoff frequency. The net result of the entire system was a charge sensitivity of 0.1 V/pC in a 80 Hz–70 kHz band [23], as shown in Fig. 11. Filtering out frequencies below 80 Hz helps to reduce unwanted 60 Hz powerline noise, as well as other low frequency noise sources, such as the bias reference. However, if desired, the low frequency bandwidth could be extended at the expense of increased noise. It is still necessary to include a dc feedback path to stabilize the charge amplifier, so the system bandwidth cannot be extended all the way to dc as currently configured.

A dc bias, generated by an ADR01 bandgap reference IC, was applied across the plates of the MEMS sensor. A passive RC low pass filter was used to reduce the noise of the reference IC output. A 100-kΩ potentiometer was used as a voltage divider to set the bias voltage anywhere from 0 to 9 V. For small deflections, the charge produced from the displacement of the sensor comes from the linearized change in capacitance multiplied by the applied

dc bias voltage,

$$Q = V_b \epsilon_0 \frac{1}{g^2} \int \int_A u(x, y) dx dy = \frac{V_b \epsilon_0}{g^2} \cdot \frac{U}{j\omega} \quad (13)$$

where $g = 7 \mu\text{m}$ is the initial sense gap, $V_b = 9 \text{ V}$ the applied bias voltage, $\epsilon_0 = 8.854 \times 10^{-12} \text{ F/m}$ is the permittivity of free space, $u(x, y)$ is the displacement of the center membrane, and the integral is over the area of that membrane. The area integral of the displacement is equal to the volume velocity, U , divided by $j\omega$. The resulting charge, Q , is passed into the charge amp and through the filter transfer function, $H(j\omega)$, to result in a final voltage output.

Pressure sensitivity measurements were carried out in an anechoic chamber using a cluster of speakers delivering 100 dB SPL at the sensor location across a 50 Hz–50 kHz band. The device under test was mounted in a hybrid leadless ceramic package as shown in Fig. 6 and inserted into a test socket on the PC board. This board was mounted inside a grounded aluminum box and placed on a tripod in the anechoic room. Power was supplied by batteries inside the box. The amplified signal from the bandpass filter output was carried by a shielded coaxial cable to a Stanford Research Systems lockin amplifier, locked to the speaker drive signal. The lockin amplifier measured the magnitude of the output signal at the drive frequency. Measurements were made at 150 logarithmically spaced frequency steps from 50 Hz to 50 kHz.

The reference pressure for the measurement was made using a Larson–Davis 2520, 0.25-in. diameter reference microphone inserted through a hole cut through the back of the grounded box and a dummy ceramic package, in an effort to create a geometry as similar as possible to the MEMS device. The reported sensitivity is the ratio of the magnitude of the voltage output of the MEMS system to the magnitude of the pressure measured by the reference microphone at each frequency step.

Fig. 12 shows these measurements for the device at 9 V bias (maximum deliverable with the current electronics) and 0.3 V

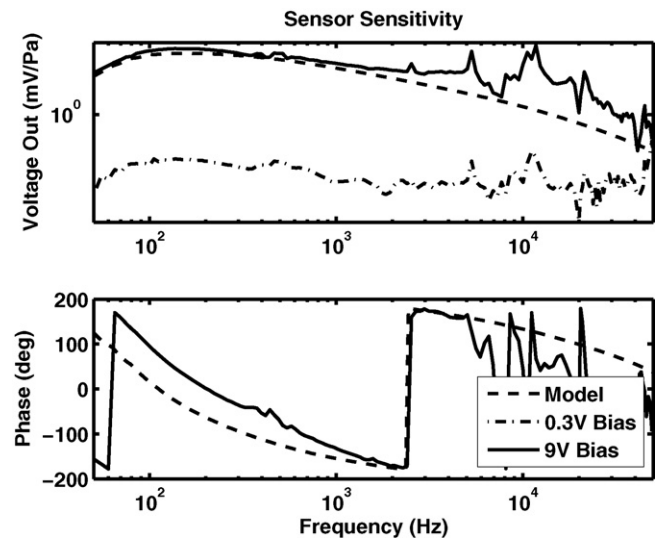


Fig. 12. Sensitivity results are shown for two bias voltages (9 and 0.3 V). The lumped element model results described above are overlaid on the plot.

bias (the voltage at which device sensitivity is minimized; see Fig. 13). At 0.3 V bias almost no acoustic sensitivity is observed; this should therefore be considered close to the noise floor of the measurement. The model results match experiment well below 3 kHz, as shown in Fig. 12. The low frequency roll-off is due to the high-pass filter on the charge amplifier, and the high frequency roll-off is due to the mechanics of the acoustic system. The system is overdamped.

Two peaks appear in the sensitivity measurement at 5 and 10 kHz which are not predicted by the model. The origin of these peaks is not certain, but they could be due to spatial variation of the sound pressure level in the test chamber (e.g., diffraction peaks from the test stand, or resonances of any cavities). Small differences between the placement of the calibration microphone and the MEMS trapped fluid microphone could then result in large differences in sensitivity, particularly at frequencies where strong spatial variation of the acoustic field is present. The module cavity size is roughly 7 cm, comparable to a wavelength at 5 kHz, and 2 wavelengths at 10 kHz; perhaps, standing waves within the module cavity are generating the sensitivity peaks. It is also possible that these peaks could be due to unmodeled higher-order modes of the fluid–structure system, such as those associated with higher-order membrane modes, compressibility of the fluid, or bulk bending of the nominally rigid silicon and glass support structures.

A plot of measured sensitivity against bias voltage for the device at a single frequency (1 kHz) is given in Fig. 13. As can be seen, the sensitivity is minimized at 0.3 V bias. The sensor output goes through a 180° phase shift as the 0.3 V point is passed. This suggests that there is a “built in” bias on the device. The “built in” bias may be a contact potential generated due to a difference in the work function of the boron doped polysilicon and platinum [24].

Linearity measurements were conducted with 9 V bias applied. The driving pressure was a 100 Hz pure tone with amplitude varying over two orders of magnitude (from 60 dB SPL to

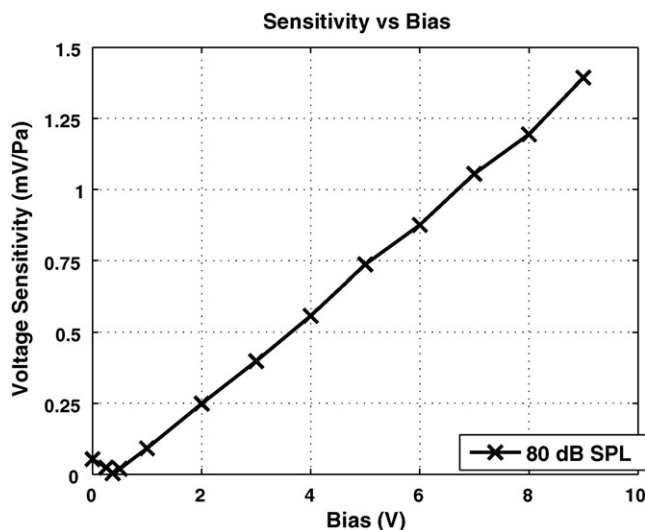


Fig. 13. Sensitivity vs. bias measurements at 1 kHz. Sensitivity reduces linearly with bias, with minimum sensitivity at 0.3 V_{bias}.

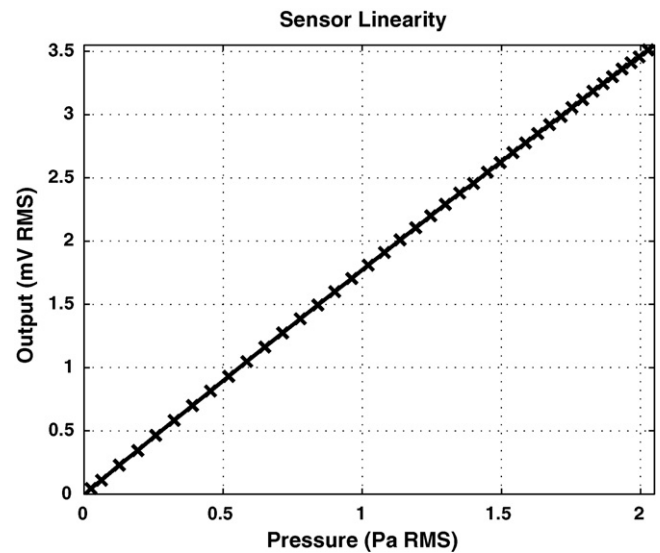


Fig. 14. Linearity measurements at 9 V_{bias}, over a range of pressure from 60 dB SPL to 100 dB SPL. The pressure is a 100 Hz pure tone.

100 dB SPL), as shown in Fig. 14. The sensor is linear over this range with a maximum deviation from linearity of 2.5%.

Noise measurements of the system output are converted into sound pressure by dividing by measured sensitivity. The results are given in Fig. 15. The total A-weighted noise with 9 V bias is 72 dBA. These measurements were conducted in an anechoic room. The anechoic room has a total ambient noise level of less than 25 dBA. Hence, all of the measured noise is coming from the electronics; indeed, reducing the bias to 0.3 V to remove any thermomechanical noise generated by the sensor itself has no effect on the measured noise. A theoretical analysis of the preamp voltage and current noise contributions, the Johnson noise of the 200 M Ω feedback resistor, and the noise contributions from the bias reference match extremely well with the

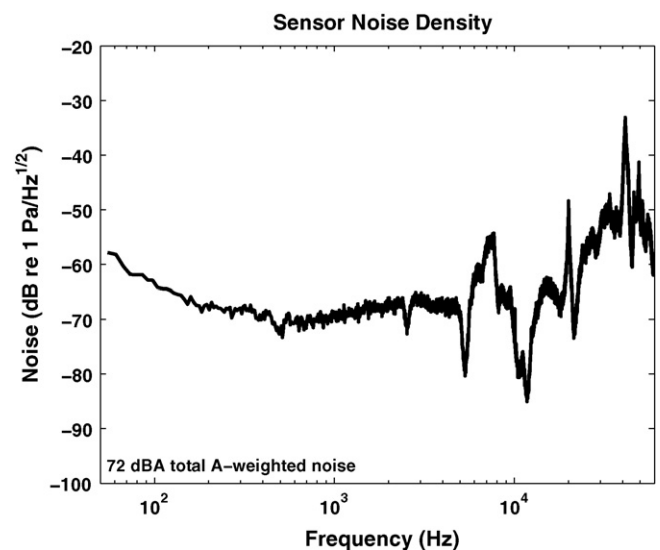


Fig. 15. Noise floor measurements conducted in an anechoic chamber. The noise floor is computed by dividing quiescent sensor output by measured sensitivity. The total A-weighted noise is 72 dBA. All of the measured noise is generated by the preamplifier electrical noise sources.

measured noise spectrum. The dominant noise sources are the Johnson noise of the feedback resistor and the voltage noise of the preamp. Hence, improving sensor noise characteristics can be addressed first by reducing the noise floor of the electronics.

6. Discussion

The microfabrication process described in this work allows the construction of an arbitrarily shaped, fluid-filled chamber bounded by arbitrarily shaped membranes. The process includes the ability to incorporate capacitive sensing and actuation between an electroded glass cap and the highly doped membrane. The fabrication process represents an advance over previous microphone processes by providing additional flexibility in the geometry of fabricated structures. The development of the process was motivated by the authors' ongoing efforts to micromachine a cochlear-analogue transducer which incorporates sensing elements, but the process is more generally applicable, and could be used to realize novel microfluidic devices and acoustic sensors.

The added flexibility achieved by the process is not without cost. The two die bonding steps at the end of the process required custom bonding jigs and were time consuming. In addition, yield was negatively impacted by devices breaking at both bonding steps. The fluidic filling process was also labor intensive, and resulted in yield loss due to membrane fracture during filling. Future work to improve the fabrication process should focus on improving these steps to increase yield.

The acoustic sensor described here as an example of the fabrication process exhibited sensitivities on par with MEMS microphones previously reported in the literature. It also served as a vehicle for demonstration of the capacitive sensing structure with the Sn–Au bonded top electrode. The flat form-factor of the system could be useful for sensing applications in space constrained environments or designs. In addition, the process allows the flexibility to design systems in which the input and sensing location are physically separated, and communicate acoustically through a trapped fluid medium. This may have advantages in environmental isolation and packaging for certain applications.

A lumped element model was effective at capturing the dynamics of this system at frequencies below 3 kHz. A thin squeeze-film damping model was accurate at predicting damping. Lumped element modeling of the fluid chamber as a combination of coupled neck masses was effective at capturing mass loading from the trapped fluid chamber. Mass loading from the external environment was unimportant. Acoustic compliance of the cavity was also unimportant, as the membrane compliance dominated. If a lower density fluid (such as air) were used to fill the cavity, the mass loading would significantly reduce, increasing bandwidth. However, the reduction in mass would most likely be accompanied by an increase in cavity compliance which would partly mitigate this effect. In addition, the radiation impedance of the environment would have a more significant effect on the system dynamics. Whether or not these are desirable outcomes depends on the intended application.

The lumped element model diverges from the experiment at frequencies above 3 kHz. This deviation is likely due to a com-

bination of unmodeled higher-order modes of the membranes, unmodeled flexibility of the Pyrex top cap or silicon support structure, and unmodeled compressibility of the fluid.

The noise floor of the example device in this paper was 72 dBA. This is high when compared to commercial microphones, and would not be acceptable for most acoustic sensing applications. Most MEMS microphones described in the literature do not report system noise floor, but the recent results of Scheeper et al. [10] indicate the ability to achieve noise floors as low as 23 dBA. Measurements indicated that in the current design, the dominant noise sources are the voltage noise of the preamplifier and the thermal noise of the feedback resistor in the preamp. Future work on improving the system noise floor should focus on the design of the preamp, or on increasing the sensitivity of the device, so as to improve the signal-to-noise ratio.

Acknowledgments

This work was supported by the National Science Foundation via a Graduate Research Fellowship, and by the Office of Naval Research. The authors would like to thank the staff of the Michigan Nanofabrication Facility for their assistance.

References

- [1] R.D. White, K. Grosh, Microengineered hydromechanical cochlear model, *Proc. Natl. Acad. Sci.* 102 (2005) 1296–1301.
- [2] R.D. White, K. Grosh, Trapped-fluid traveling wave filters based on the mammalian cochlea, in: K.F. Jensen, J. Han, D.J. Harrison, J. Voldman (Eds.), *Proceedings of the μ TAS 2005 Conference, the Ninth International Conference on Miniaturized Systems for Chemistry and Life Science*, 2005, pp. 666–668.
- [3] R.D. White, K. Grosh, Fully micromachined lifesized cochlear model, in: A.L. Nuttall (Ed.), *Auditory Mechanisms: Processes and Models*, 2006.
- [4] G. Zhou, L. Bintz, D.Z. Anderson, K.E. Bright, A life-sized physical model of the human cochlea with optical holographic readout, *J. Acoust. Soc. Am.* 93 (1993) 1516–1523.
- [5] W. Hemmert, U. Durig, M. Despont, U. Drechsler, G. Genolet, P. Vettiger, D.M. Freeman, A.W. Gummer, *A Life-sized Hydrodynamical, Micromechanical Inner Ear, Biophysics of the Cochlea: From Molecules to Models*, World Scientific, 2002, pp. 409–416.
- [6] M.J. Wittbrodt, C.R. Steele, S. Puria, Developing a physical model of the human cochlea using microfabrication methods, *Audiol. Neuro-otol.* 11 (2) (2006) 104–112.
- [7] F.Y. Chen, H.I. Cohen, T.G. Bifano, J. Castle, J. Fortin, C. Kapusta, D.C. Mountain, A. Zosuls, A.E. Hubbard, A hydromechanical biomimetic cochlea: experiments and models, *J. Acoust. Soc. Am.* 119 (1) (2006) 394–405.
- [8] P.C. Hsu, C. Mastrangelo, K.D. Wise, A high sensitivity polysilicon diaphragm condenser microphone, in: *The Proceedings of the Eleventh Annual International Workshop on MicroElectroMechanical Systems (MEMS '98)*, 1998, pp. 580–585.
- [9] W. Kuhnelt, G. Hess, A silicon condenser microphone with structured back plate and silicon nitride membrane, *Sens. Actuat. A* 30 (1991) 251–258.
- [10] P.R. Scheeper, B. Nordstrand, J. Gullov, B. Liu, T. Clausen, L. Midjord, T. Storgaard-Larsen, A new measurement microphone based on MEMS technology, *J. Microelectromech. Syst.* 12 (2003) 880–891.
- [11] P.R. Scheeper, A.G.H. vanderDonk, W. Olthius, P. Bergveld, Fabrication of silicon condenser microphones using single wafer technology, *J. Microelectromech. Syst.* 1 (1992) 147–154.
- [12] T.M.H. Lee, D.H.Y. Lee, C.Y.N. Liaw, A.I.K. Lao, I. Hsing, Detailed characterization of anodic bonding process between glass and thin-film coated silicon substrates, *Sens. Actuat. A: Phys.* 86 (2000) 103–107.

- [13] A. Goyal, J. Cheong, S. Tadigadapa, Tin-based solder bonding for MEMS fabrication and packaging applications, *J. Micromech. Microeng.* 14 (2004) 819–825.
- [14] G. Matijasevic, C.C. Lee, C.Y. Wang, Au–Sn alloy phase diagram and properties related to its use as a bonding medium, *Thin Solid Films* 223 (1993) 276–287.
- [15] C.C. Lee, C.Y. Wang, A low temperature bonding process using deposited gold-tin composites, *Thin Solid Films* 208 (1992) 202–209.
- [16] X. Zhang, T.-Y. Zhang, Y. Zohar, Measurements of residual stress in thin films using micro-rotating-structures, *Thin Solid Films* 335 (1998) 97–105.
- [17] L.L. Beranek, *Acoustics*, American Institute of Physics, Inc., New York, 1986.
- [18] J.J. Blech, On isothermal squeeze films, *J. Lubric. Technol. Trans. ASME* 105 (4) (1983) 615–620.
- [19] J.B. Starr, Squeeze-film damping in solid-state accelerometers, *Solid-State Sensor and Actuator Workshop*, 1990, pp. 44–47.
- [20] T. Veijola, H. Kuisma, J. Lahdenpera, T. Ryhanen, Equivalent-circuit model of the squeezed gas film in a silicon accelerometer, *Sens. Actuat. A. Phys.* 48 (3) (1995) 239–248.
- [21] I. Andrews, M. Harris, G. Turner, A comparison of squeeze-film theory with measurements on a microstructure, *Sens. Actuat. A. Phys.* 36 (1) (1993) 79–87.
- [22] L.E. Kinsler, A.R. Frey, A.B. Coppens, J.V. Sanders, *Fundamentals of Acoustics*, 4th ed., John Wiley and Sons, New York, NY, 2000.
- [23] P. Horowitz, W. Hill, *The Art of Electronics*, Cambridge University Press, New York, 1980.
- [24] S.M. Sze, *Physics of Semiconductor Devices*, John Wiley and Sons, New York, NY, 1969.

Biographies

Robert White received B.S. and M.S. degrees in Mechanical Engineering from the Massachusetts Institute of Technology in 1999. He worked at the C.S.

Draper Laboratories on MEMS gyroscopes from 1996 to 2000. In 2000, he entered the University of Michigan, Ann Arbor receiving a PhD in Mechanical Engineering in 2005. His doctoral research focused on adapting the ideas of cochlear mechanics to the design of lifesize micromachined cochlear models and cochlear-like sensors. Dr. White is currently an Assistant Professor of Mechanical Engineering at Tufts University, Medford, MA. His research interests include microsensors, microfabrication, and cochlear mechanics. He is a member of the Acoustical Society of America, the American Society of Mechanical Engineers, and the Institute of Electrical and Electronics Engineers.

Lei Cheng received B.S. and M.S. degrees in Engineering Mechanics from Tsinghua University, China, in 2000 and 2002, respectively. She is currently working toward the PhD degree in Mechanical Engineering at the University of Michigan. Between 2000 and 2002, her research interest was on the modeling of thermomechanical properties of short fiber reinforced metal matrix composites (MMCs). Since 2003, her research interests have been on the cochlear modeling and the design of the electroacoustic transducers. She was the recipient of a University Fellowship at Michigan.

Karl Grosh received his B.S. and M.S. degrees in Engineering Science from The Pennsylvania State University in 1985 and 1988, respectively. After working as a Research Scientist at the Naval Research Lab in Washington DC from 1987 to 1990, he attended Stanford University from 1990 to 1994 receiving his PhD in Mechanical Engineering. Since 1994, he has been a faculty member at the University of Michigan where he holds the rank Associate Professor of Mechanical Engineering with a dual appointment in Biomedical Engineering Department. Professor Grosh won the NSF Career Award (1999) and the Office of Naval Research Young Investigator Award (1999). He is a member of the Acoustical Society of America, the American Society of Mechanical Engineers, and the Association for Research in Otolaryngology. His current research interests are in cochlear mechanics, the biomechanics of growth, and the design and fabrication of electroacoustic transducers.